Dalton Transactions

Polypyrrole Coated δ-MnO2 Nanosheet Arrays as Highly Stable Lithium-ion-storage Anode

Journal:	*Dalton Transactions*
Manuscript ID	DT-ART-05-2020-001658
Article Type:	Paper
Date Submitted by the Author:	07-May-2020
Complete List of Authors:	Sui, Yiming; University of Washington, Materials Science and Engineering Liu, Chaofeng; University of Washington, Materials Science and Engineering Zou, Peichao; Tsinghua University, Division of Energy and Environment, Tsinghua Shenzhen International Graduate School Zhan, Houchao; Tsinghua University, Division of Energy and Environment, Tsinghua Shenzhen International Graduate School Cui, Yuanzheng ; Tsinghua University, Division of Energy and Environment, Tsinghua Shenzhen International Graduate School Yang, Cheng ; Tsinghua University, Division of Energy and Environment, Tsinghua Shenzhen International Graduate School Cao, Guozhong; University of Washington, Materials Science and Engineering

Polypyrrole Coated δ-MnO_2 Nanosheet Arrays as Highly Stable Lithium-ion-storage Anode

Yiming Sui,[1,2] Chaofeng Liu,[1] Peichao Zou,[2] Houchao Zhan,[2] Yuanzheng Cui,[2] Cheng Yang,[2,*] Guozhong Cao[1,*]

[1]Department of Materials Science and Engineering, University of Washington, Seattle, WA 98195, USA

[2]Division of Energy and Environment, Tsinghua Shenzhen International Graduate School, Tsinghua University, Shenzhen 518055, China

Email: Cheng Yang: yang.cheng@shenzhen.tsinghua.edu.cn, Guozhong Cao: gzcao@uw.edu

Abstract

Manganese dioxide (MnO_2) with conversion mechanism is regarded as a promising anode material for Lithium-ion batteries (LIBs) owing to its high theoretical capacity (~1223 mAh g^{-1}) and environmental benignity as well as low cost. However, it suffers from the insufficient rate capability and poor cyclic stability. To circumvent this obstacle, semiconducting polypyrrole coated-δ-MnO_2 nanosheet arrays on nickel foam (denoted as MnO_2@PPy/NF) are prepared via hydrothermal growth of MnO_2 followed with electrodeposition of PPy for anode in LIBs. The electrode with ~ 50 nm thick PPy coating exhibits an outstanding overall electrochemical performance. Specifically, a high rate capability is obtained with ~430 mAh g^{-1} of discharge capacity at a high current density of 2.67 A g^{-1} and more than 95% capacity is retained after over 120 cycles at a current rate of 0.86 A g^{-1}. These high electrochemical performances are attributed to the special structure which shortens ion diffusion pathway, accelerates charge transfer, and alleviates volume change in the charging/discharging process, suggesting a promising route on designing the conversion-type anode material for LIBs.

Keywords: Lithium-ion batteries, core-shell nanostructure, δ-MnO_2 nanosheets, poly-pyrrole coating, anodes

1 Introduction

Lithium-ion batteries (LIBs) are the most important energy storage devices and undergo rapid advancement in the past decades to meet larger demands on electric power and advanced portable electronics.[1, 2] Anode, as one critical component in LIBs, may play a determining role in the overall performances, including cyclic stability, reversible capacity, energy/power density, *etc*.[3] While the current graphite anode working with intercalation mechanism enjoyed widespread commercial success, it suffers from the limited capacity (theoretically ~372 mAh g^{-1}). It is therefore imperative to explore alternative anode materials.[4, 5]

Transition metal oxides (Fe_2O_3, V_2O_3, MnO_2, *etc.*) working with conversion mechanism can in principle deliver much higher theoretical capacity than graphite anode counterpart, even exceeding 1000 mAh g^{-1}, and also exhibit suitable working potential to achieve the goal of high energy density.[3, 6-10] Among the high-capacity anode materials, MnO_2 receives extensive attention due to its great earth abundance, low price and high theoretical capacity (1223 mAh g^{-1}).[6, 11] However, this conversion reaction involves dramatic structure/volume change, low Coulombic efficiency, and large voltage hysteresis, all of which jeopardize the overall electrochemical performances of the cells.[6] To mitigate such problems and improve their electrochemical performances, various techniques have been investigated. One strategy is by encapsulating or sandwiching manganese dioxides within conducting materials like graphene[12] and hollow carbon spheres[13] as anode composites, in which the conductive coating improves the overall electrical conductivity and provides physical confinement on volume change. However, the electrodes based on the materials are typically fabricated through the coating slurry on current collectors, in which the insulating binder hampers the rate capability by blocking the Li^+ diffusion routes and hindering the electrical conductivity.[14] Another approach is by growing nano- or micro-sized particles over 3D

conductive substrate, which could effectively shorten the diffusion route of Li^+ and increase the contact area with conducting substances in electrodes or electrolytes, which are favorable for releasing the stress generated by Li^+ insertion and promoting the rate performances and cycling stability.[15-17] However, the short cycling life of the binder-free electrodes brought by pulverization of active materials is also fatal and overshadows their advantages.[18] However, combining both strategy and fabricate conductive-materials coated binder-free MnO_2 nanomaterial electrodes could be an effective approach to circumvent the obstacles to attain high battery performance. Limited works have been reported so far on this route, partially due to the synthesis complexity of the strategy.[19-21]

In the present study, δ-MnO_2 nanosheets were in-situ grown on the surface of NF and subsequently coated with a uniform PPy layer via electrodeposition. In comparison to other methods (*e.g.* oxidative polymerization[22], vapor phase polymerization[23]), electrodeposition could not only induce the polymerization at the mild conditions without excess products or toxics but also precisely control the polymerization speed and the thickness of PPy.[24] The growth mechanism of δ-MnO_2 nanosheets, PPy deposition parameter tuning and its potential for application as anode material in LIBs have been discussed. Such structure facilitates Li^+ diffusion and withstands volume variation. It also provides large specific surface area to rapid redox reaction. PPy coating could help maintain the nanosheet integrity by offering the mechanical support and enhance the electronic conductivity.[25] Owing to the synergistic effect of nano-structured morphology of MnO_2 particles, conductive PPy coating and porous NF substrate, MnO_2@PPy/NF electrode with coating thickness of ~ 50 nm could deliver a reversible capacity of ~1240 mAh g^{-1} at 0.1 A g^{-1}, good

cycling stability with over 95% capacity retention after 120 cycles at a current rate of 0.43 A g^{-1} and capacity of ~430 mAh g^{-1} at a current density of 2.67 A g^{-1}.

2 Experimental

2.1 Synthesis of δ-MnO_2 Nanosheets on NF

The nickel foam (NF) was cut into circle disk with the radius of 5 mm, followed by supersonically cleaning for 15 minutes separately in acetone, deionized water, hydrochloric acid (3 M), and deionized water to remove the organic residues and oxide layer on the surface. Then, the cleaned NFs were dried in vacuum oven at 60 °C overnight. Thereafter, 1 mmol of $KMnO_4$ was dissolved in 20 mL of deionized water under vigorous stirring, and the as-obtained solution was transferred to 30 mL of Teflon autoclave with 3 pieces of cleaned NF immersed inside. Afterwards, the autoclave was sealed and placed in muffle oven to maintain at 180 °C for 3 hours. Finally, the resulting samples were washed with deionized water and ethanol respectively and dried at 60 °C for 24 hours. The obtained composite material was denoted as MnO_2/NF.

2.2 Electrodepositing PPy Coating

0.1 mL of pyrrole monomer was added in 10 mL of Na_2CO_3 solution (0.1 M) drop by drop under vigorous stirring. The mixture was used as electrolyte combined with MnO_2/NF working electrode, platinum counter electrode and Ag/AgCl reference electrode. The operating potential was set at 1.2 V (*vs.* Ag/AgCl) and the electrodeposition lasted for 50 s and 150 s, the corresponding products denoted as MnO_2@PPy/NF-50 and MnO_2@PPy/NF-150 separately. Subsequently, the samples were cleaned with deionized water and ethanol and dried at 60 °C in vacuum oven for 12 hours.

2.3 Materials Characterization

X-ray diffraction (XRD) was conducted by Bruker X-ray diffractometer (D8 Discover with a IμS 2-D detection system) at an accelerating voltage of 50 kV and a working current of 1000 μA, using Cu-K_α radiation source from angel 10.5 to 98.5° and initial wavelength was set at 6800 nm in order to avoid the fluorescent effect of element manganese within samples. The morphology and the size of particles were obtained via scanning electrons microscopy (SEM, Sirion XL30), atomic force microscopy (AFM) and transmission electron microscope (TEM, FEI Spirit T12). The Kratos Axis Ultra DLD X-ray photoelectron spectroscopy system (XPS) was used to confirm the surface element/bonding/valent states compositions. Burnner-Emmet-Teller (BET) via nitrogen adsorption/desorption was also employed to measure the surface area of samples. The functional groups and bonding information were collected through the Fourier transform infrared spectrometer (FT-IR, Bruker, VERTEX 70).

2.4 Electrochemical Measurements

The galvanostatic tests were conducted by using a NEWARE tester (CT-4008) between 0.01 and 3 V (*vs.* Li/Li^+), and the EIS measurements were performed with a frequency range between 10^5 and 0.01 Hz. During cell assembly, the material we studied was used as the working electrode, paired with lithium metal foil as counter electrode, 2 pieces of polypropylene film (Celgard 2400) as separator and mixed solution containing 1M $LiPF_6$ dissolved in ethyl carbonate (EC)/dimethyl carbonate (DMC) (1:1 V:V) as the electrolyte. The redox characteristics of the material was tested by cyclic voltammetry (CV) using Solartron electrochemical station (SI 1287) with a voltage window between 0.01 V and 3 V at different scan rates.

3 Results and Discussion

3.1 Material Synthesis Mechanism

Figure 1 illustrates the synthesis process of MnO_2@PPy/NF electrode. In the first step, the NF is ultrasonically washed in acetone, deionized water, hydrochloric acid, deionized, ethanol in sequence to remove the organic residue and oxide layer on surface. The cleaned NF is then immersed into $KMnO_4$ solution and undergoes hydrothermal process to grow δ-MnO_2 nanosheets on its surface. During the process, in the basic solutions (pH = 7.4 for 0.05 M $KMnO_4$ aqueous electrolyte) and at 180˚C, both the NF substrate and the water in solutions will be oxidized into NiO and O_2 respectively, and $KMnO_4$ will be reduced into MnO_2. Afterwards, the as-synthesized MnO_2/NF undergoes the electrodeposition to obtain MnO_2@PPy/NF electrode, in which the pyrrole monomers in electrolytes is induced to polymerize by external electric current and form an even PPy coating on materials surface.

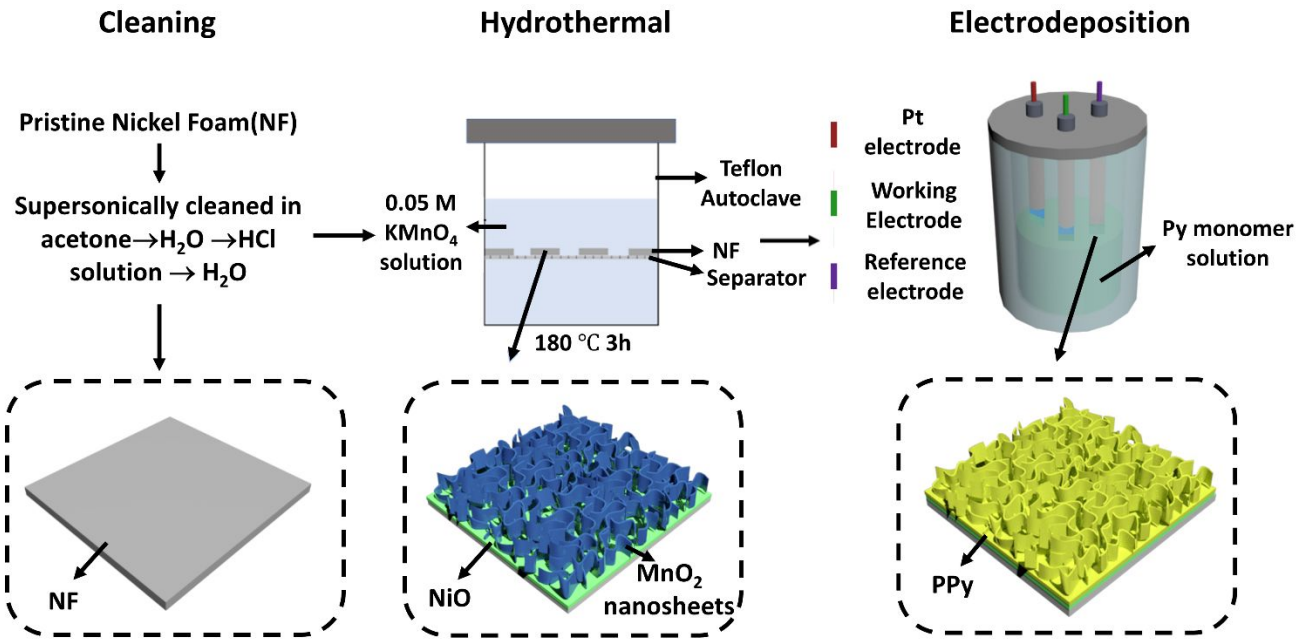

Figure 1. Schematic illustration of synthesis process of MnO_2@PPy nanosheet arrays on NF including the NF cleaning process (left), MnO_2 nanosheets growth over NF through hydrothermal process (middle) and PPy electrodeposition (right).

Two redox steps occur during the hydrothermal process as displayed in Equation 1 and 2 respectively. Firstly, both reactions are favored by thermodynamic calculation. Specifically, both redox reaction equations could be divided into two independent half reactions (*i.e.* Equation 1 $\rightarrow$ Equation 3 and Equation 4, Equation 2 $\rightarrow$ Equation 3 and Equation 5) and the standard reaction potential for two redox reactions (denoted as E_0) could be derived by adding the standard reaction potential for corresponding half reactions together.[26] Furthermore, the real potentials for two overall reactions at the working condition (denoted as E) are calculated via the classic Nernst Equation (see Equation 6) and transferred to Gibbs free energy through the Equation 7, in which R is the universal gas constant, T is the working temperature, Z is the transference number of electrons in the reaction, F is the Faraday constant and Q stands for the concentration ratio of components in the redox reaction. It turns out that the calculated Gibbs free energy values for both reactions are below zero, proving their spontaneous occurrence at the hydrothermal condition. [27-30]

$$H_2O + 2MnO_4^- + 3Ni \rightarrow 3NiO + 2MnO_2 + 2OH^- \quad \text{Eq.1}$$

$$2H_2O + 4MnO_4^- \rightarrow 4MnO_2 + 4OH^- + O_2\uparrow \quad \text{Eq.2}$$

$$MnO_4^- + 2H_2O + 3e^- \rightarrow MnO_2 + 4OH^- \qquad E_h = 0.59\,V \quad \text{Eq.3}$$

$$2OH^- + Ni - 2e^- \rightarrow NiO + H_2O \qquad E_h = 0.0874\,V \quad \text{Eq.4}$$

$$O_2 + 4e^- + 2H_2O \rightarrow 4OH^- \qquad E_h = 0.401\,V \quad \text{Eq.5}$$

$$E = E_0 - \frac{RT}{ZF}\ln(Q_R) \quad \text{Eq.6}$$

$$\Delta G = -nEF \quad \text{Eq.7}$$

In addition, the composition of the composite material (δ-MnO_2/NF) after hydrothermal reaction is also characterized by XRD, XPS, EDS and CV, and the corresponding patterns are shown in Figure 2. In XRD pattern (Figure 2a), two sharp peaks at 44.4 ^{o} and 52.1 ^{o} corresponds to the (111) and (200) planes for nickel metal substrate. The other four main peaks at 12.3 ^{o}, 24.8 ^{o}, 36.6 ^{o} and 65.5 ^{o} can be assigned to (003), (006), (101), (110) planes of birnessite-type MnO_2, respectively (PDF 00-052-0556).[26, 31] δ-MnO_2 possesses an layered structure, which is composed of octahedra MnO_6 and accommodates potassium ions between adjacent layers (Figure 2b). The missing of featured peaks for NiO phase is partially due to its low mass ratio in the composite material or the low crystallinity.[26, 31] XPS results reveal detailed information on the composition of the composites. Firstly, the broad survey scan demonstrates the coexistence of Mn, O, K, and Ni elements in the MnO_2/NF (see Figure 2c). Moreover, Mn accounts for ~ 20 at% in the composite while element Ni only accounts for ~7 at%, which partially explains the absence of featured peaks for NiO in XRD pattern. In the high-resolution Mn2p spectrum, peaks at 641.91 eV, 642.6 eV, 643.8 eV are assigned to the existence of Mn^{3+}, Mn^{4+}, Mn^{5+} (Figure 2d). To note, the existence of Mn^{3+} in MnO_2 crystals is to achieve the overall electric neutrality by compensating for the extra positive charges brought by Mn^{5+}, intercalated K^+ and oxygen vacancies.[32] The rich Mn and O vacancies in the MnO_2 crystal could tune its electronic structure and improve the electronic conductivity.[33] At the same time, the EDS pattern confirms the elements in the composite to be Mn, K, O, Ni, which coincides with the results from XPS analysis (Figure 2e). Additionally, some more information about the material composition of δ-MnO_2/NF can also be revealed by the distinct peaks in CV curve (Figure 2f). To be specific, the peaks at 1.12 V in cathodic scan and 1.9 V in anodic scan are matched with conversion reactions for NiO, which offer solid evidences

to prove the coexistence of MnO_2 and NiO.[34] To note, other electrochemical features related to the CV curves will be discussed in detail in the following sections.

In addition to thermodynamic calculation and direct characterizations on material composition, pH of solution is measured before and after the prolonged hydrothermal reaction from 3 h to 9 h and a significant increase of pH from 7.4 to 12 is noticed, which accords with the constant production of OH^- in both reactions. Besides, the products of 0.05 M $KMnO_4$ solution after hydrothermal reaction under the same experiment conditions are collected, washed, and freeze-dried. The XRD (Figure S1) and EDS (Figure S2) results prove that the material derived from $KMnO_4$ decomposition is also δ-MnO_2. Considering the mass ratio of NiO in the composite material, the MnO_2 is majorly contributed from the Equation 2. Therefore, in combination with the related literature, a general formation mechanism can be proposed.[26, 35-37] In the initial state, the surface of NF is oxidized by the $KMnO_4$ to form a composite layer of δ-MnO_2 and NiO, and this layer blocks the further reaction between bare nickel metal and the $KMnO_4$. Afterwards, the decomposition of $KMnO_4$ becomes the dominant reaction and constantly contributes MnO_2 to the previously formed MnO_2 nuclei. Finally, the δ-MnO_2 grows into thermodynamically favored nanosheets structure with slightly warped edge.[32, 35, 38]

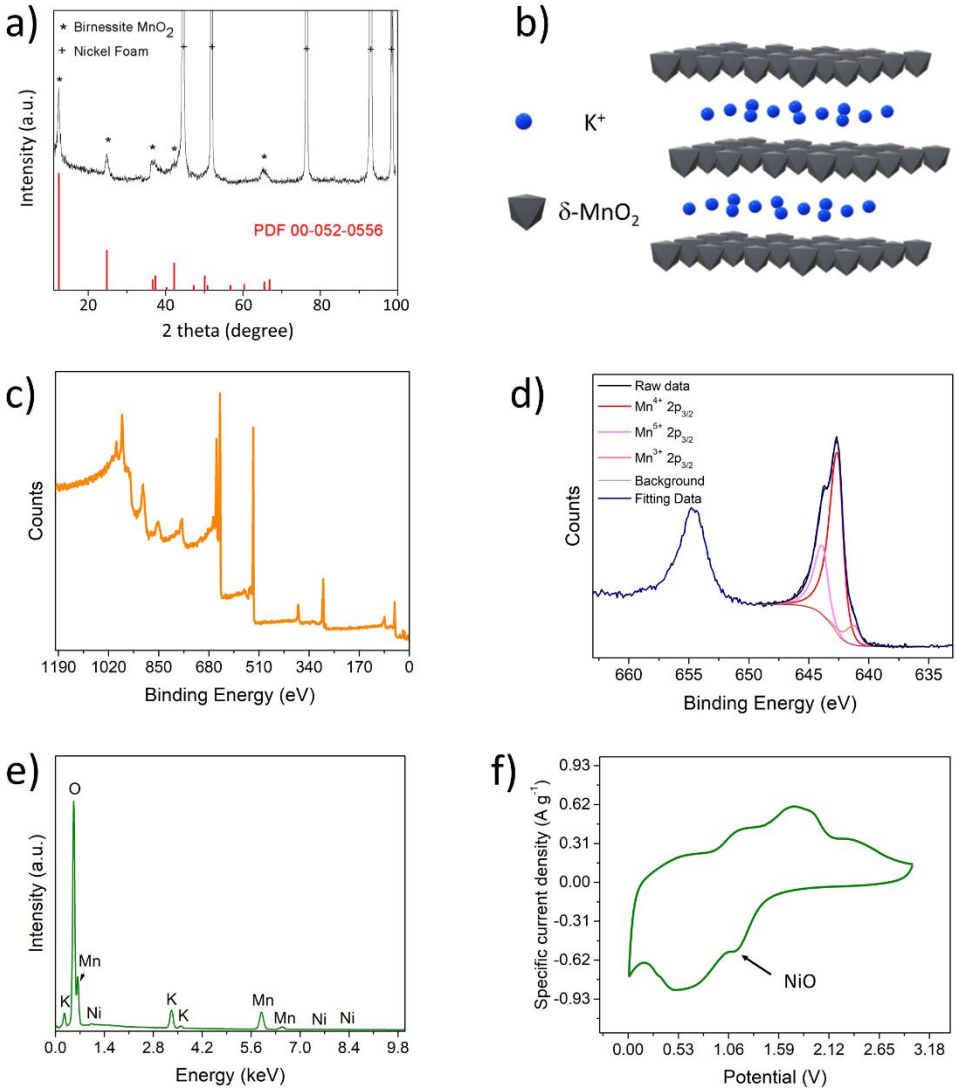

Figure 2. Structural characterization of MnO_2/NF: a) XRD pattern of the composite material. b) Schematic illustration of δ-MnO_2 structure. c) XPS survey scan. d) High resolution XPS scan of Mn $2p_{3/2}$ peaks. e) EDS pattern of the composite material. f) CV curve for the material cycling at the rate of 0.2 mV s^{-1} between 0.01 V and 3 V (*vs.* Li/Li^+).

The pyrrole monomers are electrochemically induced to polymerize on the surface of MnO_2/NF electrode and gradually form an even and uniform layer of PPy coating (affording MnO_2@PPy/NF electrode), following the reaction equation in Figure 3.[22] The electrodeposition potential is set at the 1.2 V (*vs.* Ag/AgCl) since the PPy produced with the method exhibits the optimum electric conductivity in the potential between 0.8 and 1.2 V (*vs.* Ag/AgCl).[24] Figure S3 displays the

chronoamperometric graph for the electrodeposition process (purple curve), which is distinct from the typical one on planar electrode and clearly consists of two stages with the critical time of 50 s.[39, 40] In the first stage, the Py monomers majorly polymerize on the NiO/NF substrates due to the better electric conductivity than the MnO_2 nanosheets counterparts (the green curve). The decreased current with time follows the I-$t^{1/2}$ trend, which is ascribed to the limited diffusion capability of Py monomers in electrolytes.[40, 41] In the second stage, the Py monomer polymerization over MnO_2 nanosheets counterparts begins to dominate due to the more facile supplement of the Py monomers (the orange curve). After 150 s deposition, the overall current drops to a value close to zero and maintains the constant afterwards, during which the rates of PPy growth and thickening are already very low. That is why we study the impact of PPy coating on electrochemical performances of composite electrodes with two types of samples (MnO_2@PPy/NF-50 and MnO_2@PPy/NF-150). To characterize the deposited composition, FTIR is carried out for the powder scratched from nickel foil after hydrothermal and electrodeposition. In Figure 3, the peaks at 1172 cm^{-1} and 720 cm^{-1} are from the MnO_2 in the composites[42] and the peaks at 3194 cm^{-1}, 2950 cm^{-1}, 2920 cm^{-1} and 2850 cm^{-1} correspond to hydroxyl vibration modes, 1556 cm^{-1} for antisymmetric pyrrole ring vibration, 1480 cm^{-1} for symmetric pyrrole ring vibration, peaks at 1403 cm^{-1}, 1330 cm^{-1}, 1259 cm^{-1} for the C-N stretching vibration, 1095 cm^{-1} for =C-H, 1038 cm^{-1} for N-H in-plane deformation vibration, 958 cm^{-1} for out-of-plane vibration of C-H, 878 cm^{-1} and 798 cm^{-1} for out-of-plane deformation vibration of C-H,[24, 25, 43-46] conforming the formation of PPy coating.

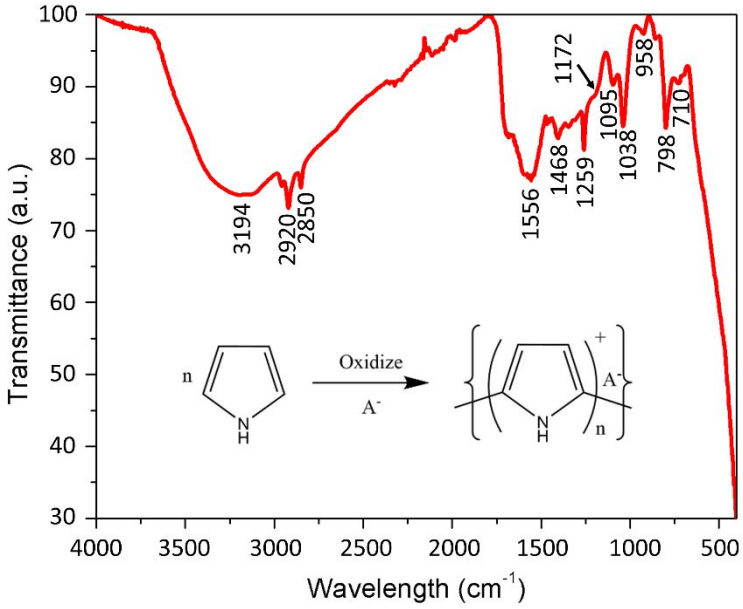

Figure 3. FTIR spectrum of the MnO_2@PPy/NF sample (the inset is the reaction equation of pyrrole monomer polymerizing into PPy).

3.2 Microstructure

The materials with different PPy depositing time are characterized by FE-SEM and AFM. The NF substrate exhibits smooth surface, in comparison with the rough surface morphology after *in-situ* growing the MnO_2 nanosheets and depositing the PPy coating (see Figure S4-6 and Figure 4a-f). Besides, high magnification SEM and AFM images of bare MnO_2/NF sample (Figure 4b, c) also display the clear warped edge for the nanosheets, which has already been discussed above. After the PPy electrodeposition and extension of deposition time, the material surface gets rougher (Figure S5, 6 and Figure 4e, f), which partially reflects the successful deposition of PPy coating. Furthermore, TEM is carried out for both the bare MnO_2 nanosheets and MnO_2@PPy nanosheets at the deposition time of 150 s, which are prepared by separately scratching them off the nickel substrate directly after the hydrothermal and electrodeposition. As shown in Figure 4g, the hierarchical structure could be directly observed with the thickness of PPy coating approximately 40-50 nm at the electrodeposition time of 150 s. Under the high resolution TEM (HRTEM), the

distance between adjacent lattice is ~ 0.24 nm which is in agreement with spacing of (111) plane of δ-MnO_2 (Figure 4h), again demonstrating the composition of nanosheets to be δ-MnO_2.[26]

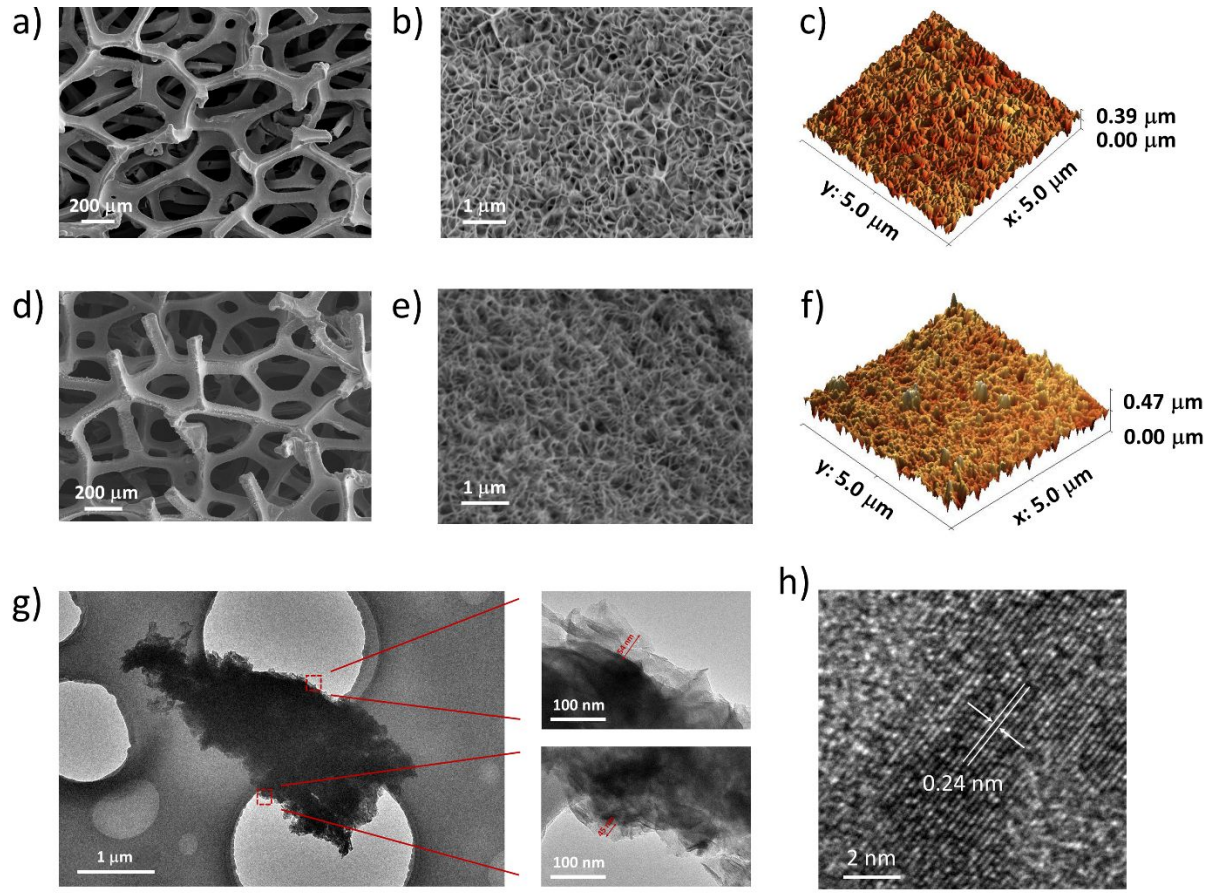

Figure 4. a-c) Microstructure characterizations of MnO_2/NF sample: a) SEM image at low magnification, b) SEM image at higher magnification and c) 3D AFM image. d-f) Microstructure characterizations of MnO_2@PPy/NF-150 sample undergoing 150 s PPy electrodeposition: d) SEM image at low magnification, e) SEM image at higher magnification and f) 3D AFM image. g) TEM image of MnO_2@PPy/NF. h) HRTEM image of MnO_2/NF.

3.3 Electrochemical Performances

The electrochemical lithium storage performances of the as-synthesized material (MnO_2@PPy/NF) was first evaluated through galvanostatic charge/discharge testing at the rate of 83 mA g^{-1} at the potential range between 0.01 V and 3.0 V (*vs.* Li/Li^+). The initial three cycling curves are displayed

in Figure 5a. In the initial cycle, a discharge capacity of approximately 2038 mAh g^{-1} is calculated, which is much higher than the theoretical capacity of MnO_2 (1230 mAh g^{-1}) and the delivered capacities in the following cycles, leading to the low Coulombic efficiency of 60%. This extra capacity is assumed from the decomposition of electrolytes and the further formation of SEI layer on anode material surface.[35, 47] In the 2nd and 3rd cycle, the curve overlaps and Coulombic efficiency quickly increases to over 90%, suggesting prominent reversibility and stability of the electrochemical reactions. Meanwhile, the initial three cycles of CV curves are also measured within voltage window of 0.01-3 V (*vs.* Li/Li^+) at the scan rate of 0.2 mV s^{-1} to characterize the featured redox reactions and their corresponding potentials during the cycling process (Figure 5b). In the first cathodic scan, there are several strong and broad peaks below 1.2 V, which are significantly reduced in the following cycles, partially due to the SEI layer formation.[48] In addition, clear peak at ~0.4 V in cathodic scan and two peaks at ~1.2 V and 2.3 V in anodic scan represent for redox reactions for manganese dioxide, which corresponds to the reversible reaction as shown in Equation 7,[20, 35] while the peaks at 1.12 V in cathodic scan and 1.9 V in anodic scan are matched with conversion between NiO and Ni which has been mentioned above.[34] To estimate the capacity contribution of NF substrate and the PPy coating, similar amount of PPy is electrodeposited over the equal-size NF substrate with a mass loading of ~0.1 mg cm^{-2}, of which the CV curve is also measured between 0.01-3 V *vs.* Li/Li^+ at the scan rate of 0.2 mV s^{-1} (Figure 5c). By comparing the occupied area, the PPy and NF only accounts for < 3% capacity in the composite material of MnO_2@PPy/NF via the redox reactions on PPy, which is similar to the reported results in literatures.[47]

$$MnO_2 + 4Li^+ + 4e^- \Leftrightarrow 2Li_2O + Mn \qquad \text{Eq.7}$$

$$NiO + 2Li^+ + 2e^- \Leftrightarrow Li_2O + Ni$$

Eq.8

The charge transfer resistance of electrodes was measured via electrochemical impedance spectroscopy (EIS). As shown in Figure 5d and Figure S7, Nyquist plots of bare MnO_2/NF, δ-MnO_2@PPy/NF-50 and δ-MnO_2@PPy/NF-150 electrodes exhibit similar trends, but the MnO_2@PPy/NF-150 electrode with larger amount of PPy coating presents smaller charge transfer resistance due to the superior electrical conductivity of PPy itself, which benefits to the faster reaction kinetics. MnO_2@PPy/NF-150 electrode unveiled an excellent capacity retention at severe conditions as displayed in Figure 5e. To be specific, the cells undergo the galvanostatic charging/discharging for 5 cycles at every current rate of 0.08 A g^{-1}, 0.17 A g^{-1}, 0.33 A g^{-1}, 0.67 A g^{-1}, 1.33 A g^{-1}, 2.67 A g^{-1}, 0.08 A g^{-1}, 0.83 A g^{-1} in sequence. Notably, high discharge capacities of ~623 mAh g^{-1} and 430 mAh g^{-1} are reserved at high current densities of 1.33 A g^{-1} and 2.67 A g^{-1}, respectively. In addition to the conductive PPy coating on surface, the highly porous structure allowed by the well aligned MnO_2 nanosheets over nickel foam results in drastically shortened diffusion distance of Li^+ and consequently contributes to the superior rate capability of the composite electrodes. To note, despite of the observed decreasing resistance with addition of PPy in EIS results, the rate performances at the current density from 0.08 to 1.3 A g^{-1} don't have many changes. As the EIS test is conducted directly after 12 h of cells assembling, the results may indicate that the electrical conductivity before galvanostatic test is not the key limiting factor on the rate capability of the material, while other issues like SEI formation or material phase transformation process should be considered. In comparison, the much increased capacity is observed with the extension of cycles when returning to the rate to 0.08 A g^{-1} and 0.83 A g^{-1}, suggesting enhanced reversibility and stability brought by the PPy coating (Figure 5e and Figure

S7). Furthermore, the long-term cycling performance of the bare MnO_2/NF, MnO_2@PPy/NF-150 and MnO_2@PPy/NF-50 electrodes are displayed in Figure 5f and Figure S8 separately. To note, all these electrodes are firstly pre-cycled at 0.08 A g^{-1} for 5 cycles to form a high-qualify SEI layer (stable and even distributed) on their surface. For bare MnO_2/NF electrode, it confronts severe capacity decay, rapidly dropping from 1000 mAh g^{-1} to 20 mAh g^{-1} in the first 80 cycles. In comparison, MnO_2@PPy/NF-50 delivered a better cycling stability, with over 69% capacity retention at the 120th cycles relative to the 6th cycle while MnO_2@PPy/NF-150 electrodes further improve the cyclic stability, with trivial capacity decay in first few cycles and keeping constant in the following cycles and delivered an overall capacity retention of over 95% (~ 930 mAh g^{-1}). This improvement could be ascribed to the improved mechanical and electronic properties of PPy coating and better coverage with extension of electrodeposition time, which mechanically suppresses the pulverization of particles and further prevents the loss of active mass during the conversion reaction with large volume expansion.[49, 50] Hence, electrochemical depositing PPy is supposed to be the optimum parameter to achieve the optimum electrochemical performances from the perspectives of charge transfer resistance, rate capability and cyclic stability. Notably, the performances of the composite MnO_2@PPy/NF electrode in our work are comparable and even exceed those of previously reported MnO_2-based anode materials as summarized in Table 1, demonstrating the superiority of our hierarchical structure design in comparison to merely conductive coating or porous structure counterparts.

Table 1. Electrochemical performances of designed anode material in this work and ones reported in previous works.

Anode Material	Cyclic Stability	Rate Capability	Reference

MnO_2 nanorods/ rGO	~103% of the initial capacity (~600.3 mAh g^{-1}) at 0.5 A g^{-1} for 650 cycles	811 mAh g^{-1} at 0.1 A g^{-1}, 242.4 mAh g^{-1} at 2 A g^{-1}	[51]
Mesoporous MnO_2	~94% of the initial capacity (~260 mAh g^{-1}) at 1 A g^{-1} for 200 cycles	905 mAh g^{-1} at 0.1 A g^{-1}, 135 mAh g^{-1} at 2 A g^{-1}	[52]
MnO_2 nanoparticles	~75% of the initial capacity (~813 mAh g^{-1}) at 0.1 A g^{-1} for 100 cycles	1095 mAh g^{-1} at 0.1 A g^{-1}, 464 mAh g^{-1} at 2 A g^{-1}	[53]
MnO_2 nanorods/ rGO	~70% of the initial capacity (~595 mAh g^{-1}) at 0.1 A g^{-1} for 60 cycles	726 mAh g^{-1} at 0.1 A g^{-1}, 380 mAh g^{-1} at 2 A g^{-1}	[54]
MnO_2/C hybrid sphere	~99% of the initial capacity (~803 mAh g^{-1}) at 1 A g^{-1} for 60 cycles	1104 mAh g^{-1} at 0.1 A g^{-1}, 354 mAh g^{-1} at 2 A g^{-1}	[55]
MnO_2@PPy/NF	~95% of the initial capacity (~930 mAh g^{-1}) at 0.42 A g^{-1} for 120 cycles	~1240 mAh g^{-1} at 0.1 A g^{-1}, ~430 mAh g^{-1} at 2.7 A g^{-1}	This work

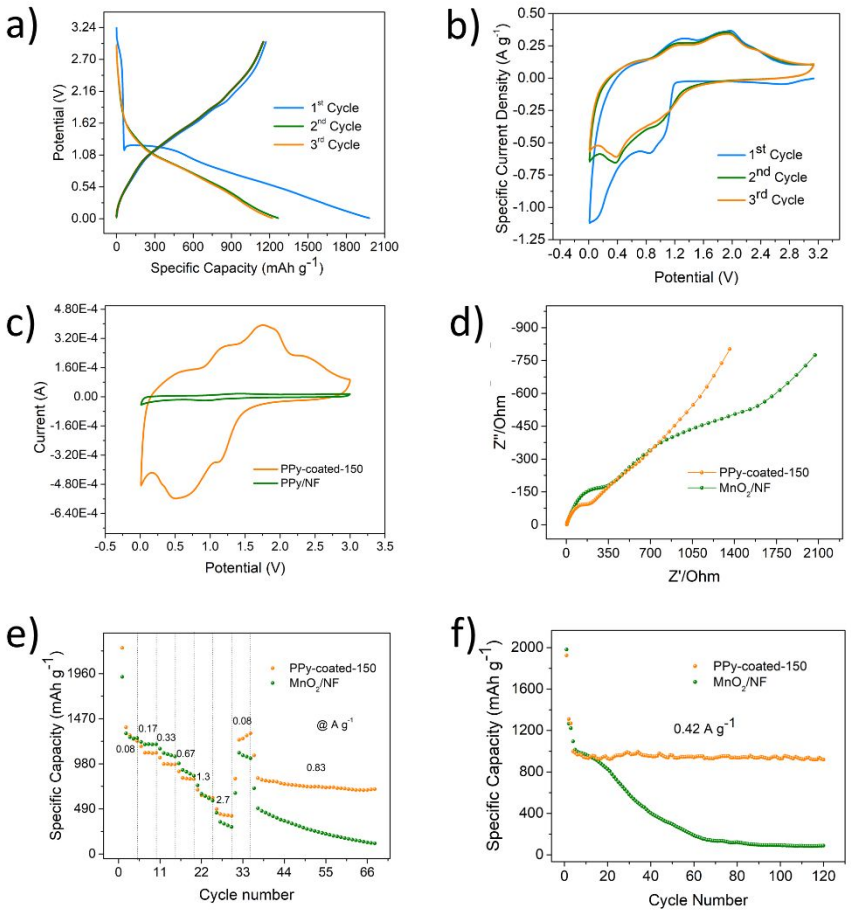

Figure 5. a) Galvanostatic charging/discharging curves of MnO_2@PPy/NF-150 electrode during the first three cycles at the current density of 0.08 A g^{-1}. b) Cyclic Voltammetry curves of MnO_2@PPy/NF-150 electrode during the first three cycles at the fixed sweeping rate of 0.2 mV s^{-1}. c) CV curves of the MnO_2@PPy/NF-150 (black line) and the PPy coated NF (red line) at the same rate of 0.2 mV s^{-1}. d) Electrochemical impedance spectra of the bare MnO_2/NF electrodes (black line) and MnO_2@PPy/NF-150 electrodes (blue line) in the frequency range of 100 kHz – 0.01 Hz. e) Rate capacities of different composite electrodes at various current densities. f) Cycling performance of the bare MnO_2/NF electrodes (black line) and MnO_2@PPy/NF-150 electrodes (blue line) at the current density of 0.42 A g^{-1}.

Pseudocapacitive behavior of MnO_2@PPy/NF-150 is discussed through analyzing the cyclic voltammetry curves at different scan rates at the voltage window from 0.01 V to 3 V (*vs.* Li/Li^+), as shown in Figure 6a. The positively shifted peaks in cathodic scan and negatively moved peaks in anodic scan with increasing scan rates reveal the larger polarization for featured electrochemical reactions at higher rates. Furthermore, with the help of equation $i = av^b$, the capacity contribution from capacitive effect can be figured out, in which the i and v denote current value and the scan

rate, respectively, *a* is a constant which is short for several parameters and parameter *b* reflects the originality of major capacity contribution, with *b* close to 0.5 indicating an intercalation predominating process while *b* close to 1 indicating a capacitive predominating one.[56] As the *b* value for most selected points is less than 0.75, insertion/de-insertion process other than capacitive process make the dominant contribution to the overall capacity. Furthermore, by applying Equation $\frac{\mathrm{i(V)}}{v^{\frac{1}{2}}} = K_1 v^{1/2} + k_2$, in which former term represents for current contribution from ion intercalation and later one corresponds to the current contribution from surface capacitive effect, the capacitive capacity contribution ratio under different scan rates is figured out and summarized in Figure 6b and Figure 6c. To be specific, the pseudocapacitive capacity contribution at the rate of 0.2, 0.3, 0.5, 0.8, 1.2, 1.5 mV s^{-1} are 24%, 27%, 32%, 38%, 43%, 49% separately. This suggests the increasing importance of pseudocapacitive effect in electrochemical performances at the higher sweeping rates as a result of the limitation of Li^+ diffusion capability in electrolytes, which to some extent contributes to the superior rate capability of the composite material at larger rates.[56]

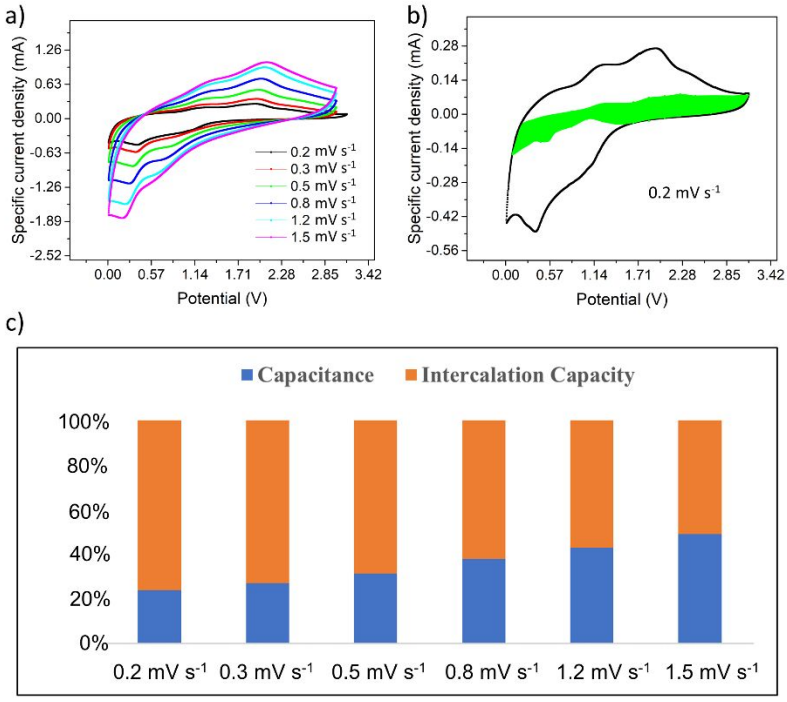

Figure 6. Comparison of a) CV curves at different current rates. b) CV curve of the composite MnO_2@PPy/NF-150 electrode with separation between the overall current (black line) and pseudocapacitive current (light green area). c) Comparison of the pseudocapacitive contribution in overall capacity at different sweeping rates.

4. Conclusions

Highly porous MnO_2@PPy/NF-150 anode was synthesized using hydrothermal growth of MnO_2 nanosheets over NF followed by electrodeposition of PPy on surface. As anodes for LIBs, the composite material delivered good cycling performance with ~ 970 mAh g^{-1} capacity at 0.42 A g^{-1} and remaining 95% capacity after over 120 cycles, as well as good rate capability with ~430 mAh g^{-1} discharging capacity presented at the high current density of 2.67 A g^{-1}, which are competitive and even surpassing those reported MnO_2-based anode materials. To count, the synergistic effects of the conductive PPy coating, nanosheets morphology and 3D conductive hosts help buffer the severe volume variation of MnO_2 during conversion reaction and achieve such a good cyclic stability, suggesting a promising route on designing the anode material for LIBs

Acknowledgements

This work was supported by the National Science Foundation (CBET 1803256), the Local Innovative and Research Teams Project of Guangdong Pearl River Talents P rogram (2017BT01N111) and Shenzhen Government (Project No. JCYJ20170412171720306 & JSGG20170414143635496).

References

1. Vazquez, S., et al., *Energy Storage Systems for Transport and Grid Applications.* IEEE Transactions on Industrial Electronics, 2010. **57**(12): p. 3881-3895.
2. Sui, Y., et al., *Dual-ion batteries: The emerging alternative rechargeable batteries.* Energy Storage Materials, 2020. **25**: p. 1-32.
3. Nitta, N., et al., *Li-ion battery materials: present and future.* Materials Today, 2015. **18**(5): p. 252-264.
4. DiVincenzo, D.P. and E.J. Mele, *Cohesion and structure in stage-1 graphite intercalation compounds.* Physical Review B, 1985. **32**(4): p. 2538-2553.
5. Jiang, J. and J.R. Dahn, *Effects of solvents and salts on the thermal stability of LiC6.* Electrochimica Acta, 2004. **49**(26): p. 4599-4604.
6. Yu, S.H., et al., *Conversion Reaction-Based Oxide Nanomaterials for Lithium Ion Battery Anodes.* Small, 2016. **12**(16): p. 2146-2172.
7. Wang, M.-S., et al., *Scalable preparation of porous micron-SnO2/C composites as high performance anode material for lithium ion battery.* Journal of Power Sources, 2016. **309**: p. 238-244.
8. Liu, H., et al., *Rational design of TiO2@ nitrogen-doped carbon coaxial nanotubes as anode for advanced lithium ion batteries.* Applied Surface Science, 2018. **458**: p. 1018-1025.
9. Zhu, C., et al., *TiO2 nanotube @ SnO2 nanoflake core–branch arrays for lithium-ion battery anode.* Nano Energy, 2014. **4**: p. 105-112.
10. Mahmood, N., T. Tang, and Y. Hou, *Nanostructured Anode Materials for Lithium Ion Batteries: Progress, Challenge and Perspective.* Advanced Energy Materials, 2016. **6**(17): p. 1600374.
11. Reddy, M.V., G.V. Rao, Subba, and B.V.R. Chowdari, *Metal oxides and oxysalts as anode materials for Li ion batteries.* Chemical Reviews, 2013. **113**(7): p. 5364-5457.
12. Li, L., A.-R.O. Raji, and J.M. Tour, *Graphene-Wrapped MnO2–Graphene Nanoribbons as Anode Materials for High-Performance Lithium Ion Batteries.* Advanced Materials, 2013. **25**(43): p. 6298-6302.
13. Zang, J., et al., *Hollow carbon sphere with open pore encapsulated MnO2 nanosheets as high-performance anode materials for lithium ion batteries.* Electrochimica Acta, 2018. **260**: p. 783-788.
14. Yu, N., et al., *In-situ growth of binder-free hierarchical carbon coated CoSe2 as a high performance lithium ion battery anode.* Applied Surface Science, 2019. **483**: p. 85-90.

15. Jia, B., et al., *Construction of MnO2 Artificial Leaf with Atomic Thickness as Highly Stable Battery Anodes.* Advanced Materials, 2020. **32**(1): p. 1906582.
16. Guo, C.X., et al., *A Hierarchically Nanostructured Composite of MnO2/Conjugated Polymer/Graphene for High-Performance Lithium Ion Batteries.* Advanced Energy Materials, 2011. **1**(5): p. 736-741.
17. Qin, J., et al., *MnOx/SWCNT macro-films as flexible binder-free anodes for high-performance Li-ion batteries.* Nano Energy, 2013. **2**(5): p. 733-741.
18. Fu, S., et al., *Hydrogenation Driven Conductive Na2Ti3O7 Nanoarrays as Robust Binder-Free Anodes for Sodium-Ion Batteries.* Nano Letters, 2016. **16**(7): p. 4544-4551.
19. Li, Y., et al., *Free-standing reduced graphene oxide/MnO2–reduced graphene oxide–carbon nanotube nanocomposite flexible membrane as an anode for improving lithium-ion batteries.* Physical Chemistry Chemical Physics, 2017. **19**(11): p. 7498-7505.
20. Zhou, X., et al., *Embedding MnO2 Ultrafine Nanoparticles within Graphene-Based Hybrid Elastomer as an Anode for Enhanced Lithium Storage.* ChemElectroChem, 2018. **5**(16): p. 2310-2315.
21. Gao, T., et al., *Biomass-Derived Carbon Paper to Sandwich Magnetite Anode for Long-Life Li-Ion Battery.* ACS Nano, 2019. **13**(10): p. 11901-11911.
22. Bi, W., et al., *V2O5–Conductive polymer nanocables with built-in local electric field derived from interfacial oxygen vacancies for high energy density supercapacitors.* Journal of Materials Chemistry A, 2019. **7**(30): p. 17966-17973.
23. Chen, Y.-s., et al., *Gas sensitivity of a composite of multi-walled carbon nanotubes and polypyrrole prepared by vapor phase polymerization.* Carbon, 2007. **45**(2): p. 357-363.
24. Lim, Y.S., et al., *Polypyrrole/graphene composite films synthesized via potentiostatic deposition.* Journal of Applied Polymer Science, 2013. **128**(1): p. 224-229.
25. Han, L., P. Tang, and L. Zhang, *Hierarchical Co3O4@PPy@MnO2 core–shell–shell nanowire arrays for enhanced electrochemical energy storage.* Nano Energy, 2014. **7**: p. 42-51.
26. Ren, Z., et al., *Large-scale synthesis of hybrid metal oxides through metal redox mechanism for high-performance pseudocapacitors.* Scientific Reports, 2016. **6**(1): p. 20021.
27. Petrucci, R.H., Harwood, W. S. & Herring, F. G, *General Chemistry: Principles and Modern Applications*. 2002, Prentice Hall: Englewood Cliffs.
28. Lide, D.R., *Handbook of Chemistry and Physics*. 2004, CRC Press LLC: Boca Raton.
29. R.W. Bosch, D.F., and J.P. Celis, *Electrochemistry in Light Water Reactors*. 2007: CRC Press.
30. Conzuelo, F., et al., *The Open Circuit Voltage in Biofuel Cells: Nernstian Shift in Pseudocapacitive Electrodes.* Angewandte Chemie International Edition, 2018. **57**(41): p. 13681-13685.
31. Saha, S., et al., *In-situ hydrothermal synthesis of MnO2/NiO@Ni hetero structure electrode for hydrogen evolution reaction and high energy asymmetric supercapacitor applications.* Journal of Energy Storage, 2016. **6**: p. 22-31.
32. Zhao, Y., et al., *Defect-Engineered Ultrathin δ-MnO2 Nanosheet Arrays as Bifunctional Electrodes for Efficient Overall Water Splitting.* Advanced Energy Materials, 2017. **7**(18): p. 1700005.
33. Cheng, X.-B., et al., *Toward Safe Lithium Metal Anode in Rechargeable Batteries: A Review.* Chemical Reviews, 2017. **117**(15): p. 10403-10473.
34. Varghese, B., et al., *Fabrication of NiO Nanowall Electrodes for High Performance Lithium Ion Battery.* Chemistry of Materials, 2008. **20**(10): p. 3360-3367.
35. Liu, H., et al., *Reduced graphene oxide anchored with δ-MnO2 nanoscrolls as anode materials for enhanced Li-ion storage.* Ceramics International, 2016. **42**(12): p. 13519-13524.
36. Chen, H., et al., *One-Step Fabrication of Ultrathin Porous Nickel Hydroxide-Manganese Dioxide Hybrid Nanosheets for Supercapacitor Electrodes with Excellent Capacitive Performance.* Advanced Energy Materials, 2013. **3**(12): p. 1636-1646.

37. Yan, D., et al., *Fabrication, In-Depth Characterization, and Formation Mechanism of Crystalline Porous Birnessite MnO2 Film with Amorphous Bottom Layers by Hydrothermal Method.* Crystal Growth & Design, 2009. **9**(1): p. 218-222.
38. Xie, X., et al., *Controlled Fabrication of High-Quality Carbon Nanoscrolls from Monolayer Graphene.* Nano Letters, 2009. **9**(7): p. 2565-2570.
39. Garfias-García, E., et al., *Mechanism and kinetics of the electrochemical formation of polypyrrole under forced convection conditions.* Journal of Electroanalytical Chemistry, 2008. **613**(1): p. 67-79.
40. Saidman, S.B. and J.B. Bessone, *Electrochemical preparation and characterisation of polypyrrole on aluminium in aqueous solution.* Journal of Electroanalytical Chemistry, 2002. **521**(1): p. 87-94.
41. Grzeszczuk, M., J. Kalenik, and A. Kępas-Suwara, *Phase boundaries in layer-by-layer electrodeposited polypyrrole resulted from 2D–3D growths of polymer sublayers.* Journal of Electroanalytical Chemistry, 2009. **626**(1): p. 47-58.
42. Mylarappa, M., et al., *A facile hydrothermal recovery of nano sealed MnO2particle from waste batteries: An advanced material for electrochemical and environmental applications.* IOP Conference Series: Materials Science and Engineering, 2016. **149**: p. 012178.
43. Sultana, I., et al., *Electrodeposited polypyrrole (PPy)/para (toluene sulfonic acid) (pTS) free-standing film for lithium secondary battery application.* Electrochimica Acta, 2012. **60**: p. 201-205.
44. Li, J., L. Cui, and X. Zhang, *Preparation and electrochemistry of one-dimensional nanostructured MnO2/PPy composite for electrochemical capacitor.* Applied Surface Science, 2010. **256**(13): p. 4339-4343.
45. Liang, K., et al., *In situ synthesis of SWNTs@MnO2/polypyrrole hybrid film as binder-free supercapacitor electrode.* Nano Energy, 2014. **9**: p. 245-251.
46. Aigbe, U.O., et al., *Removal of hexavalent chromium from wastewater using PPy/Fe3O4 magnetic nanocomposite influenced by rotating magnetic field from two pole three-phase induction motor.* Journal of Physics: Conference Series, 2018. **984**: p. 012008.
47. Hashmi, S.A., A. Kumar, and S.K. Tripathi, *Investigations on electrochemical supercapacitors using polypyrrole redox electrodes and PMMA based gel electrolytes.* European Polymer Journal, 2005. **41**(6): p. 1373-1379.
48. Gou, W., et al., *Yolk-shell structured V2O3 microspheres wrapped in N, S co-doped carbon as pea-pod nanofibers for high-capacity lithium ion batteries.* Chemical Engineering Journal, 2019. **374**: p. 545-553.
49. Liu, J., et al., *Three dimensionals α-Fe2O3/polypyrrole (Ppy) nanoarray as anode for micro lithium ion batteries.* Nano Energy, 2013. **2**(5): p. 726-732.
50. Liu, J., et al., *Uniform Hierarchical Fe3O4@Polypyrrole Nanocages for Superior Lithium Ion Battery Anodes.* Advanced Energy Materials, 2016. **6**(13): p. 1600256.
51. Ma, Z. and T. Zhao, *Reduced graphene oxide anchored with MnO2 nanorods as anode for high rate and long cycle Lithium ion batteries.* Electrochimica Acta, 2016. **201**: p. 165-171.
52. Voskanyan, A.A., C.-K. Ho, and K.Y. Chan, *3D δ-MnO2 nanostructure with ultralarge mesopores as high-performance lithium-ion battery anode fabricated via colloidal solution combustion synthesis.* Journal of Power Sources, 2019. **421**: p. 162-168.
53. Zhang, L., et al., *Tailoring nanostructured MnO2 as anodes for lithium ion batteries with high reversible capacity and initial Coulombic efficiency.* Journal of Power Sources, 2018. **379**: p. 68-73.
54. Liu, H., et al., *MnO2 nanorods/3D-rGO composite as high performance anode materials for Li-ion batteries.* Applied Surface Science, 2017. **392**: p. 777-784.
55. Wang, G., et al., *Constructing Hierarchically Hollow Core–Shell MnO2/C Hybrid Spheres for High-Performance Lithium Storage.* Small, 2016. **12**(29): p. 3914-3919.

56. John Wang, J.P., James Lim, Bruce Dunn, *Pseudocapacitive Contributions to Electrochemical Energy Storage in TiO2 (Anatase) Nanoparticles.* Journal of Physical Chemistry C, 2007. **111**(40): p. 14925-14931.